Design principles for self-forming interfaces enabling stable lithium-metal anodes

Yingying Zhu[a,1], Vikram Pande[b,1], Linsen Li[a,c,2], Bohua Wen[c], Menghsuan Sam Pan[c], David Wang[c], Zi-Feng Ma[a], Venkatasubramanian Viswanathan[c,2], and Yet-Ming Chiang[c,2]

[a]Department of Chemical Engineering, Shanghai Electrochemical Energy Devices Research Center, Shanghai Jiao Tong University, Shanghai 200240, China; [b]Department of Mechanical Engineering, Carnegie Mellon University, Pittsburgh, PA 15213; and [c]Department of Materials Science & Engineering, Massachusetts Institute of Technology, Cambridge, MA 02139

Edited by Alexis T. Bell, University of California, Berkeley, CA, and approved September 15, 2020 (received for review February 1, 2020)

The path toward Li-ion batteries with higher energy densities will likely involve use of thin lithium (Li)-metal anode (<50 μm thickness), whose cyclability today remains limited by dendrite formation and low coulombic efficiency (CE). Previous studies have shown that the solid–electrolyte interface (SEI) of the Li metal plays a crucial role in Li-electrodeposition and -stripping behavior. However, design rules for optimal SEIs are not well established. Here, using integrated experimental and modeling studies on a series of structurally similar SEI-modifying model compounds, we reveal the relationship between SEI compositions, Li deposition morphology, and CE and identify two key descriptors for the fraction of ionic compounds and compactness, leading to high-performance SEIs. We further demonstrate one of the longest cycle lives to date (350 cycles for 80% capacity retention) for a high specific-energy Li||$LiCoO_2$ full cell (projected >350 watt hours [Wh]/kg) at practical current densities. Our results provide guidance for rational design of the SEI to further improve Li-metal anodes.

batteries | lithium metal anode | solid-electrolyte interface | electrolytes

Matching high-voltage oxide cathodes (>4 V vs. Li^+/Li) with thin lithium (Li) metal (<50 μm in thickness) anodes promises Li-ion batteries with specific energies exceeding 350 watt hours (Wh) kg^{-1} (1). However, the cycle life of thin Li-metal anodes is severely limited by short-circuits (i.e., "sudden death") caused by Li-dendrite formation and low coulombic efficiency (CE) as a result of side reactions between Li metal and electrolyte (i.e., "gradual death") (2–4). Recently published work has shown that dendrite formation may be suppressed to some extent by employing three-dimensional (3D) current collectors (5, 6), functionalized separators (7–9), electrolyte additives (10–13), Li-surface coatings (14–17), concentrated electrolytes (18–21), and solid electrolytes (22–24). With such improvements, it becomes urgent to address the low-CE problem, for otherwise "gradual death" (running out of available Li or electrolyte dry-out) would likely occur before "sudden death" (short-circuit), and limit the cycle life.

Li metal is highly reductive and reacts instantaneously with electrolyte constituents upon contact to form a surface film generally referred to as the solid–electrolyte interface (SEI) (25, 26). SEI formation consumes active Li^+ ions and leads to coulombic inefficiency. To minimize such loss, it is necessary for the SEI formation reaction to be self-limiting. It has also been shown recently that the microstructure and properties of SEIs can impact the crystal growth behavior of Li metal during electrodeposition (charging of the cell) (13, 27) and how the Li deposits are stripped during battery discharge (28). Therefore, SEI tuning may be a promising strategy for improving Li-metal anode performance. A variety of compounds, such as Li_3PO_4 (15), LiF (29, 30), LiBr (31), LiI (32), $LiNO_3$ (33), Li_2S_8 (34), AlI_3 (35), SnI_2 (36), Al_2O_3 (37), and Cu_3N (38), have been used to modify the SEI and shown to be effective in improving the cycling performance of Li-metal anode. However, these studies were usually conducted with Li-metal anodes of larger thickness (usually >250 μm, i.e., large Li excess). For high energy density, feasibility must be demonstrated with thin Li-metal anode (≤50 μm, small Li excess), which demands high CE to ensure long cycle life. To date, it has been quite challenging to achieve stable cycling >300 cycles when thin Li-metal anode (≤50 μm) is used. It also appears that SEI tuning often follows a trial-and-error approach that results in incremental improvement and slow progress. Thus, it is necessary to establish clear selection criteria for effective SEI modifiers.

Here, we first quantify the impact of Li-metal anode thickness and CE on specific-energy density and cycle life of Li-metal rechargeable batteries. Then, using a model series of structurally similar SEI-modifying compounds, we show the interrelationship between SEI compositions, Li deposition behavior, and CE. We identify two key descriptors (i.e., ionicity and compactness) for high-performance SEIs using integrated experimental and modeling studies. Using this approach, electrolytes that result in a highly ionic and compact SEI enriched with LiF and sulfites have been discovered, which promotes formation of a dense Li film during electrodeposition and achieve both dendrite-free and high-CE cycling (up to 99.1% for Li-metal anode). Li (50 μm)||$LiCoO_2$ (areal capacity ~4.2 milliampere hours [mAh] cm^{-2}) full

Significance

It is possible to nearly double the energy density of existing lithium-ion batteries by using lithium metal anodes. However, it has been known for decades that the lithium dendrites and mossy lithium formed during charging (electrodeposition) limit the cycle life of the batteries. It is important to change the growth behavior of lithium metal, which is closely related to the properties of the solid–electrolyte interface (SEI) formed via spontaneous reactions between the lithium metal and the electrolyte. In this experimental-modeling integrated study, we reveal the design principles of the SEI that facilitates the dendrite-free and dense deposition of lithium and demonstrate one of the best cycling performances of lithium metal anode to date under practically relevant conditions.

Author contributions: L.L., V.V., and Y.-M.C. conceived and supervised the research; Y.Z. and L.L. performed the experiments with assistance from B.W., M.S.P., D.W., and Z.-F.M.; V.P. carried out the DFT simulations and analysis; and V.P., L.L., V.V., and Y.-M.C. wrote the manuscript with assistance from all authors.

Competing interest statement: V.P., L.L., V.V., and Y.-M.C. are inventors on US provisional patent application 15/480,235 submitted by the Massachusetts Institute of Technology that relates to electrolyte additives and self-formed separators enabling lithium metal anodes.

This article is a PNAS Direct Submission.

[1]Y.Z. and V.P. contributed equally to the work.

[2]To whom correspondence may be addressed. Email: linsenli@sjtu.edu.cn, venkvis@cmu.edu, or ychiang@mit.edu.

This article contains supporting information online at https://www.pnas.org/lookup/suppl/doi:10.1073/pnas.2001923117/-/DCSupplemental.

First published October 15, 2020.

cells demonstrate stable cycling exceeding 350 cycles (to 80% capacity retention) at practical coulombic rates (C-rates) (0.2 C charge/0.5 C discharge, 1 C = 3.7 mA cm^{-2}). For even thinner Li-metal anodes (20 μm thickness), full cells still cycle for 130 cycles. Our results provide guidance for rational selection and optimization of SEI modifiers to advance development of high energy-density and long-cycle life Li-metal rechargeable batteries.

Results and Discussion

Impact of Electrode Thickness and CE on Specific-Energy Density and Cycle Life of Li-Metal Batteries. The calculated specific-energy density and cycle life of Li-metal batteries consisting of a high areal capacity $LiCoO_2$ cathode (4.2 mAh cm^{-2}) and a Li-metal anode of various thicknesses (i.e., 20-μm-thick Li corresponds to 4.12 mAh cm^{-2}) are shown in Fig. 1. The fraction of Li passed per cycle (F_p) can be calculated from the areal capacity of the cathode and the anode:

$$F_p = \frac{Q_{cathode}}{Q_{cathode} + Q_{Li}}. \quad [1]$$

Here, $Q_{cathode}$ and Q_{Li} are the areal capacities of the cathode and Li-metal anode, respectively; F_p varies inversely with the percentage of Li excess of the battery, and, naturally, the battery reaches its highest energy density in the anode-free case, $F_p = 1$. Thus in Fig. 1, the gravimetric/volumetric energy density decreases as Fp decreases (Li excess increases), with the energy density being calculated based on the total mass and volume of the cathode, anode, current collectors, separator, and liquid electrolyte and including a packaging factor, as detailed in the *SI Appendix*. The cycle life of the battery, n, may be predicted based on the CE_{avg} of the battery, which is the CE averaged over the number of cycles until all of the Li from the Li-metal anode and 20% of the Li from the cathode (i.e., $Q_{Li} + 0.2 \times Q_{cathode}$) runs out (i.e., 80% capacity retention for the battery). CE_{avg} is calculated as follows:

$$CE_{avg} = 1 - \left(\frac{Q_{Li} + 0.2Q_{cathode}}{n}\right) \times \left(\frac{1}{Q_{Li\ passed\ per\ cycle}}\right)$$
$$= 1 - \frac{Q_{Li} + 0.2Q_{cathode}}{nQ_{cathode}}. \quad [2]$$

$(Q_{Li} + 0.2 \times Q_{cathode})/n$ *is* the average Li loss per cycle. Therefore, the average CE loss per cycle is $(0.2 \times Q_{cathode} + Q_{Li})/n$ divided by $Q_{Li\ passed\ per\ cycle}$. Here, if we assume charging to 100% state-of-charge, and that CE loss occurs only at the Li-metal anode, not at the cathode, $Q_{Li\ passed\ per\ cycle}$ can be considered to be equivalent to $Q_{cathode}$ during cycling. From Eqs. **1** and **2**, the relation between F_p and cycle life (n) can be determined as:

$$F_p = \frac{1}{n(1 - CE_{avg}) + 0.8}. \quad [3]$$

The F_p vs. n plots in Fig. 1 are constructed based on Eq. **3** at several selected values of CE_{avg} ranging from 80 to 99.99%. As shown in Fig. 1, if the CE_{avg} is as low as 80%, the battery cannot survive more than 60 cycles even with a 250-μm-thick Li-metal anode (low F_p, large Li excess). With a CE_{avg} of 99.9%, even an anode-free battery can last 200 cycles; when a thin Li-metal anode (e.g., 20 or 50 μm) is employed, the cycle life of the Li-metal battery can be further increased to more than 1,160 cycles or 2,640 cycles, respectively, approaching the cycle life of existing Li-ion batteries using graphite anodes. Due to the low density of Li metal (0.534 g cm^{-3}), this only leads to a small reduction in gravimetric energy density but a large reduction in volumetric energy density. Thus, the increase in the thickness of the Li-metal foil improves the cycle life but at the cost of gravimetric/volumetric energy density. In this work, we demonstrate cycling of Li-metal batteries using Li-metal foils with 20- and 50-μm thickness.

Selecting SEI Modifiers. The central theme of this work is to establish the selection criteria for SEI modifiers that create a stable Li-metal anode interface and one that has the potential to self-heal upon formation of cracks. The spontaneous reaction between Li metal and iodine (I_2), which is historically used in primary batteries and leads to the formation of a Li^+-conducting layer and solid separator during operation (39), offers a starting paradigm. However, due to the shuttle reactions associated with $I^-/I_3^-/I_2$, this limits the voltage capability of cathodes to less than 3.2 V (40, 41). Similar shuttle reactions are present for other halide species involving bromide and chloride at potentials below that of 4-V cathodes (such as $LiCoO_2$ and $LiNi_xMn_yCo_zO_2$) (42). Among the halide series, this criterion leaves only LiF; the benefits of a LiF-rich SEI have been documented before (12, 18, 19, 30, 43). However, direct addition of LiF as a salt in common organic electrolytes is not possible due to its extremely limited solubility (<0.002 mM in dimethyl carbonate [DMC], as measured by plasma emission spectroscopy). Therefore, we focused on the approach whereby LiF-rich SEIs are formed through intentional decomposition of fluorinated electrolyte constituents at the Li-metal surface. Density-functional theory (DFT) calculations were used to probe reactions of a wide range of fluorinated organic compounds and Li-metal surface to determine their propensity to form a desired SEI (*SI Appendix*, Fig. S1). Note that these compounds can be considered either as (co)solvents or additives depending on the amount added into the electrolyte.

We focused our study on a series of structurally similar fluorinated organic compounds, namely fluoroethylene carbonate (FEC), difluoroethylene carbonate (DFEC), and 3,3,3-trifluoropropylenecarbonate (also known as trifluoromethyl ethylene carbonate [CF_3EC]) (see molecular structure in Fig. 2*A*). The result from ethylene carbonate (EC) is also included for

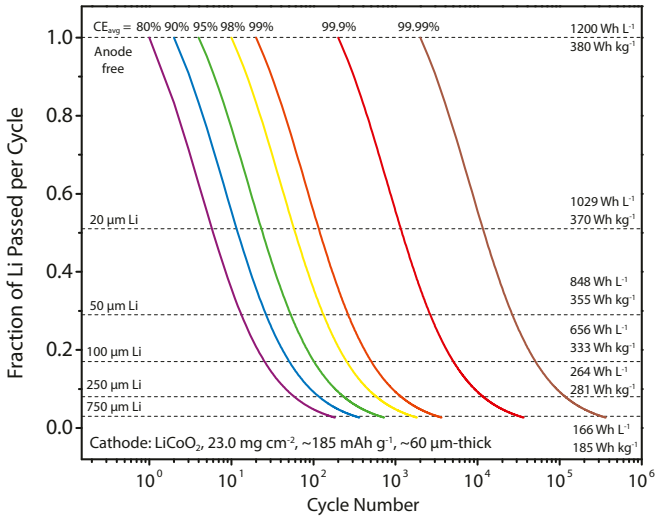

Fig. 1. Prediction of energy density and cycle life of Li-metal batteries. The gravimetric energy density, volumetric energy density, and cycle life are functions of the average CE (CE_{avg}) and fraction of Li passed (F_p) per cycle according to Eq. **3**. The total mass and volume of the electrodes, current collectors, separator, electrolyte, and packaging are included in the calculation of gravimetric and volumetric energy density respectively, as detailed in *SI Appendix*. The 20-, 50-, 100-, 250-, and 750-μm-thick Li-metal films are chosen because they are commercially available.

comparison. FEC is known to decompose to produce LiF at the Li surface and significantly improve Li-metal cycling (12, 30, 43–45). DFEC has been reported to produce LiF at the surface of graphite (46) and SiO/C anodes (47) but has not been applied to Li-metal anodes. Despite the improved cycling performance of Li-metal anodes in FEC-containing electrolytes, a molecular basis for selection of high-performing electrolytes is still missing. The formation of LiF-rich SEIs has been suggested to enhance performance (12, 30, 45). Within this simple picture, one would expect DFEC and CF_3-EC to function similarly or perhaps even better, as they are structurally similar to FEC and contain more F atoms per molecule. This work aims to build a fundamental molecular basis for selecting high-performing electrolytes for Li-metal anodes through a combination of computational and experimental studies.

In order to develop insights into the decomposition of these organic compounds on the Li-metal surface, we first perform DFT calculations that show that FEC spontaneously decomposes to form LiF, unstable CO^- anion and Li salt of glycolaldehyde (Fig. 2 *B* and *C*). DFEC decomposes partially upon ring opening, leading to formation of LiF and a large Li alkoxide. Interestingly, CF_3EC, despite containing more F in its molecular structure, does not decompose to form LiF, according to our DFT calculations. These results clearly show that not every fluorinated organic solvent decomposes to form LiF at the Li-metal surface. During the screening process for SEI modifiers, we also explored another approach to enriching LiF in the SEI, whereby the F atoms are extracted from the electrolyte salt $LiPF_6$. It was previously reported that trace amounts of H_2O could trigger the decomposition of $LiPF_6$ to produce a LiF-rich SEI (13). However, good cycling performance of the Li anode was not achieved. We discovered that 1,3,2-dioxathiolan-2,2-oxide (DTD) (see molecular structure in Fig. 2*A*) decomposes along with $LiPF_6$ to form LiF, PF_5, ethane-1,2-diolate (similar to a decomposition product of FEC), and SO_2^{2-} anion (Fig. 2 *B* and *C*). DTD was previously studied as an additive for lithium nickel–manganese–cobalt (NMC)-graphite batteries and it could reduce cell impedance (48).

To corroborate the DFT calculations, X-ray photoelectron spectroscopy (XPS) measurements were made to probe the SEIs of Li films deposited in electrolytes containing 1 M $LiPF_6$ dissolved in EC-DMC (EL-0), FEC-DMC (EL-1), DFEC-DMC (EL-2), CF_3EC-DMC (EL-3), and FEC-DMC + 3 wt% DTD (EL-4). Approximately the same amount of Li (~4.2 mAh cm^{-2}) was deposited on Li/Cu substrates (50-μm-thick Li, 15-μm-thick Cu) by charging Li (50 μm)||$LiCoO_2$ cells to 4.5 V at 0.1 C. The deposited Li films were rinsed with fresh DMC and dried under an argon atmosphere before transferring to XPS measurements using an air-proof sample holder. Wide-scan XPS spectra of the SEIs (Fig. 2 *D* and *E* and *SI Appendix*, Table S1) show that the F content in the SEI increases in the order of EL-0 (1.5 atm%), EL-3 (1.7 atm%), EL-1 (5.8 atm%), EL-4 (7.2 atm%), and EL-2 (10.6 atm%), which is in agreement with the trend predicted by the DFT calculations. Narrow-scan XPS spectra of F, C, and O are analyzed, and the results are summarized in Fig. 2 *F*, *G*, and *H*, respectively. The F 1s spectra for all five SEIs show similar peaks that can be assigned to LiF and $Li_xP_yF_z$ or C-F (Fig. 2*F*). Interestingly, unlike the other cases, there is much more $Li_xP_yF_z$ (79.8%) than LiF (20.2%) in the SEI formed in EL-2 (1 M $LiPF_6$ DFEC-DMC). A similar observation was made recently for DFEC decomposition at the SiO/C-anode surface (47). The high intensities of the C-O peaks in the C 1s spectra (Fig. 2*G*) and ROLi peak in the O 1s spectra (Fig. 2*H*) observed for the SEIs formed in EL-2 and EL-3, but not in EL-1 and EL-4, support the results from DFT simulations that DFEC and CF_3EC do not decompose as completely as FEC. According to the O 1s spectra (Fig. 2*G*), ROLi species are formed when FEC and DFEC are used, while a large amount of alkyl Li carbonate ($ROCO_2Li$) is observed when CF_3EC is used. It is also observed in EL-4 that the presence of DTD in FEC-DMC promotes the formation of Li_2CO_3 over ROLi (compare EL-4 and EL-1).

For EL-4, the S 2p spectrum was also collected and analyzed. Surprisingly, there are few S-containing species (0.1 atm%) observed at the surface of the Li film deposited in the first cycle (Fig. 2*D* and *SI Appendix*, Fig. S2). This may be explained by the decomposition rate of DTD vs. FEC at Li surface. DFT calculations suggest that FEC decomposes directly on Li while DTD codecomposes with $LiPF_6$. Thus we may expect the DTD decomposition reaction to be slower. Once the Li-metal surface is passivated by the decomposition products of FEC (such as LiF), its reactivity toward DTD or other molecules is significantly reduced (*SI Appendix*, Fig. S3). On the Li-metal surface that was cycled 10, 20, and 50 times, $ROSO_2Li$ and Li_2SO_3 were indeed observed (*SI Appendix*, Fig. S2). Therefore, S-containing species were gradually incorporated into the SEI during Li-deposition/-stripping cycles. These results indicate the potential for systematically tuning the inorganic and organic content in the SEI through spontaneous reactions between the organic electrolyte constituents and Li metal.

SEI and Li-Metal Electrodeposition Behaviors. To investigate the relationship between SEI composition and Li-metal electrodeposition behavior, scanning electron microscopy (SEM) was performed on the Li film deposited in EL-0, EL-1, EL-2, EL-3, and EL-4 electrolytes using Li (50 μm)||$LiCoO_2$ cells at 0.1 C (~0.37 mA cm^{-1}). The SEM used for this study was installed inside an argon-filled glovebox, so that the samples were never exposed to air. Top-view SEM images showed that Li particles of several microns were deposited in EL-0, EL-1, and EL-4 (Fig. 3*A*, *B*, and *E*). Smaller Li particles were observed in EL-2 (Fig. 3*C*) and EL-3 (Fig. 3*D*). The difference in Li-electrodeposition behavior among the five electrolytes is more clearly seen in the cross-sectional SEM images in Fig. 3 *F*–*J*. The deposited Li films were clearly thicker in the EL-0 (~35 μm) and EL-3 electrolytes (~37 μm) than EL-1 (~24 μm), EL-4 (~27 μm), and EL-2 electrolytes (~28 μm), despite having the same areal capacity or areal mass. There was little variation in the thickness of the deposited Li films when the roller-pressed $LiCoO_2$ electrodes were used as the counter electrode and Li source. The deposited Li films were relatively flat. However, when a thick Li foil was used as the counter electrode instead of the $LiCoO_2$ electrodes, the surface of the deposited Li film was uneven (*SI Appendix*, Fig. S4). Unlike the roller-pressed $LiCoO_2$ electrodes that undergo a small volume change during charging, the Li metal at the surface of the Li-foil counter electrode was constantly dissolving, which likely led to the different Li-electrodeposition behavior.

Since the deposited capacity of 4.2 mAh cm^{-2} corresponds to a thickness of ~20 μm if we assume that the Li film is fully dense, we can estimate the compactness of the deposited Li film using the thickness of the deposited Li observed in cross-sectional SEM. The deposited Li film is 57% compact in EL-0, 83% in EL-1, 71% in EL-2, 54% in EL-3, and 74% in EL-4. It appears that the LiF-rich SEIs formed in the EL-1 and EL-4 electrolytes promote the deposition of dense Li films and with particle-like Li morphology. According to previous literature (18, 49), this morphology often corresponds to a high CE. It has been shown that whisker-like Li particles are prone to cracking during stripping and thereby lose contact to become "dead Li" (28), which likely leads to a low CE. We also studied the Li-deposition behavior at higher current densities (0.5, 1, and 2 C). As the current density increases, the size of the deposited Li particles becomes smaller. The Li particles become more fiber-like as well (*SI Appendix*, Fig. S5).

Li-CE Measurements. After the study into the initial Li deposition (Figs. 2 and 3), we moved on to investigate the effect of the different SEI modifiers in long-term electrodeposition/stripping cycles, which may be best quantified in terms of the average CE

of Li-metal anode ($CE_{avg\text{-}Li}$). In order to accurately measure $CE_{avg\text{-}Li}$, it is necessary to have a limited Li source, so that the loss of working Li can be traced. This can be done with a full cell using an intercalation cathode, but any losses at the positive electrode may be difficult to separate from those occurring at the Li-metal electrode. We developed an asymmetric Li-Li cell test that is able to accurately quantify the $CE_{avg\text{-}Li}$ occurring over a number of cycles (Fig. 4*A*). The asymmetric cell consists of two Li-metal electrodes, one of which has a low areal capacity that is systematically consumed during cycling. In the present study, we used a 20-μm-thick Li film coated on a copper foil (Q_{Li} = 4.12 mAh cm^{-2}) as this working electrode, while the counter electrode is a 750-μm-thick Li foil with a large excess of capacity. The two electrodes were assembled into a coin cell with a polyethylene

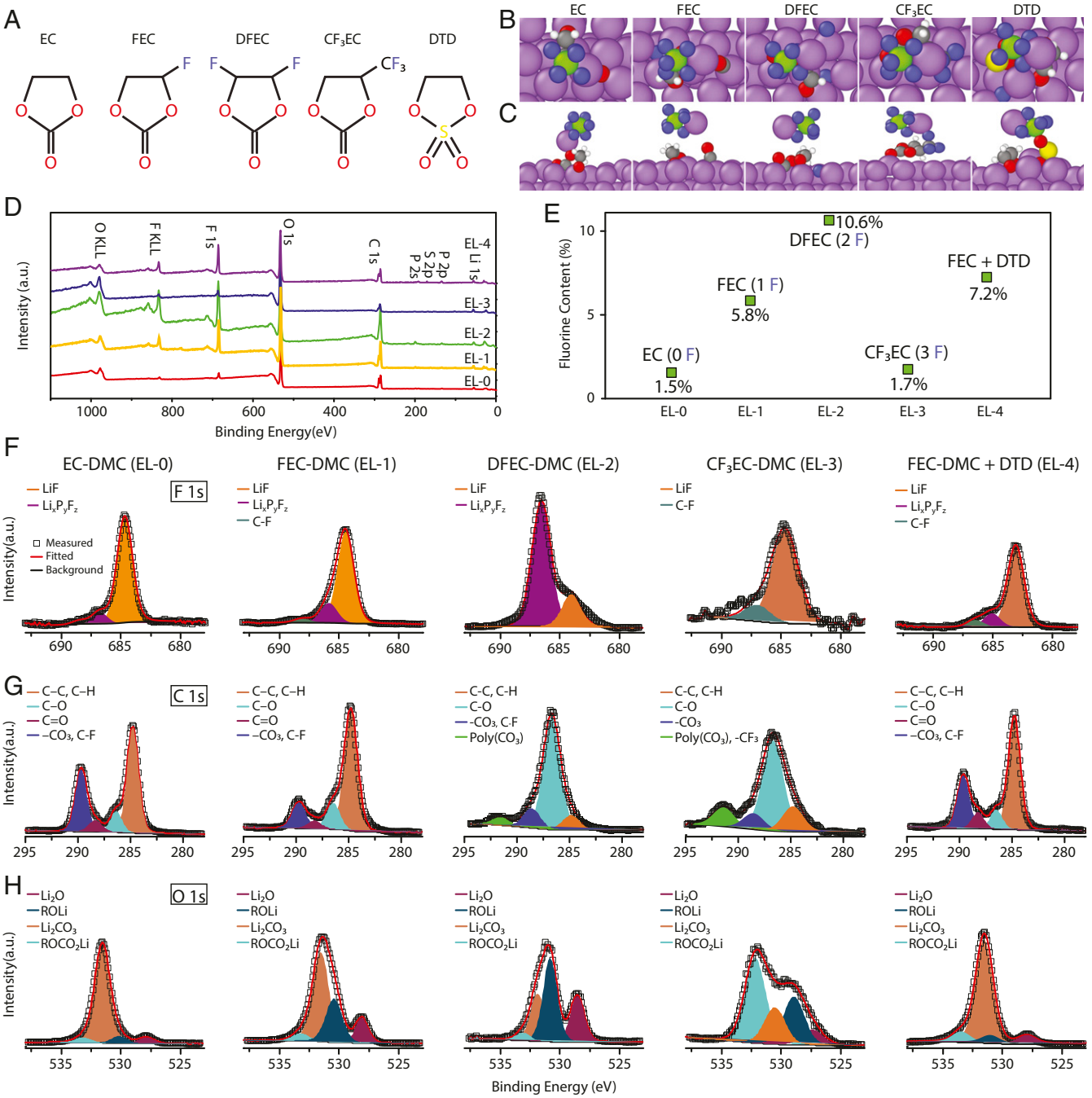

Fig. 2. Decomposition of selected molecules at the Li surface studied by DFT calculations and XPS. (*A*) Molecular structure of EC, FEC, DFEC, CF_3EC, and DTD. *B* and *C* are top and side views, respectively, of final decomposition products of EC, FEC, DFEC, CF_3EC, and DTD at Li (100) surface in the presence of $LiPF_6$, as predicted by DFT calculations. The purple atoms represent Li, red represent O, gray represent C, green represent P, blue represent F, yellow represent S, and silver represent H. FEC and DTD break down completely, while DFEC decomposes partially and CF_3EC does not undergo significant breakdown. DTD also catalyzes the decomposition of $LiPF_6$, leading to formation of LiF. (*D*) Wide-scan XPS spectra collected from the surface of the Li film deposited in 1 M $LiPF_6$ EC-DMC (EL-0), 1 M $LiPF_6$ FEC-DMC (EL-1), 1 M $LiPF_6$ DFEC-DMC (EL-2), 1 M $LiPF_6$ CF_3EC-DMC (EL-3), and 1 M $LiPF_6$ FEC-DMC + DTD (EL-4). (*E*) F content at the surface of the Li film deposited in different electrolytes. F content increases in the order of EL-3, EL-0, EL-1, EL-4, and EL-2. *F–H* are narrow-scan XPS spectra of F 1s, C 1s, and O 1s, showing that DFEC and CF_3EC decompose differently from FEC, despite their structural similarity. a.u., arbitrary units.

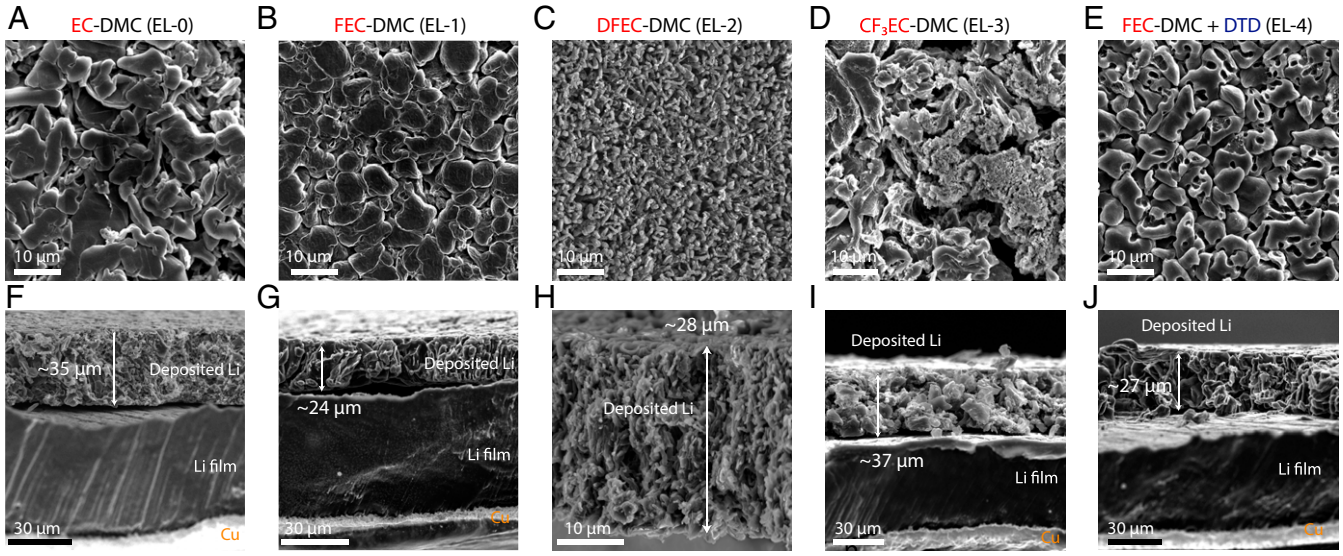

Fig. 3. SEM characterization of the deposited Li film on the Li/Cu substrates. *A–E* are top-view SEM images of the deposited Li films on the Li/Cu substrates (50-μm-thick Li, 15-μm-thick Cu) in 1 M $LiPF_6$ EC-DMC (EL-0), 1 M $LiPF_6$ FEC-DMC (EL-1), 1 M $LiPF_6$ DFEC-DMC (EL-2), 1 M $LiPF_6$ CF_3EC-DMC (EL-3), and 1 M $LiPF_6$ FEC-DMC + DTD (EL-4), respectively. The Li films were deposited in $LiCoO_2$-Li cells by charging at 0.1 C to 4.5 V vs. Li^+/Li. The same amount of Li (~4.2 mAh cm^{-2}) was deposited for all five cases. Microsized Li particles were observed in EL-0, -1, and -4. Smaller particles were observed in EL-3. *F–J* are the corresponding cross-sectional SEM images. The thickness of the deposited Li layer increases in the order of EL-1, EL-4, EL-2, EL-0, and EL-3.

separator and liquid electrolyte. In the first half-cycle, a known amount of Li, in this instance, 3.0 mAh cm^{-2} (Q_{Li} passed per cycle), is deposited on the thin working electrode (here, at a current density of 0.6 mA cm^{-2}). The same 3.0 mAh cm^{-2} is then stripped from the working electrode. With each successive cycle, the same Q_{Li} passed per cycle is stripped and plated. Any coulombic inefficiency erodes the initial 20-μm-thick Li film on the working electrode. Barring a short-circuit event, the original thin Li electrode is gradually consumed by side reactions, either forming an SEI or being isolated by an SEI during cycling and forming so-called "dead Li" (Fig. 4*B*) (50). When all of the initial Li at the working electrode is consumed, a voltage spike is generally observed. Three selected examples are shown in Fig. 4*C*. Crucially, the appearance of voltage spike (denoted by the black arrows in Fig. 4*C*) shows that short-circuits are absent. If it takes N cycles for the 20-μm-thick Li-film working electrode to be fully consumed, the average CE over N cycles can be calculated using the following equation:

$$\mathrm{CE}_{avg-Li} = 1 - \frac{Q_{Li}}{NQ_{Li\ passed\ per\ cycle}}. \qquad [4]$$

Here, the Q_{Li}/N is the average Li loss per cycle. Therefore, the average CE loss per cycle is Q_{Li}/N divided by $Q_{Li\ passed\ per\ cycle}$.

We first tested the effectiveness of this approach by measuring the CE_{avg-Li} of the thin Li anodes in several selected electrolytes reported in previous literature. The results are summarized in *SI Appendix*, Table S2. Different values of CE_{avg-Li} were clearly observed for different electrolytes. The Li-metal anodes were reported to cycle well in 1 M lithium bis(trifluoromethanesulfonyl) imide (LiTFSI) EC/tetrahydropyran (51), 1 M $LiAsF_6$ EC/2-methyl-tetrahydropyran (52), and 1 M LiTFSI 1,3-dioxolane/1,2-dimethoxyethane (DME) (1:1 vol/vol) + 1 wt% $LiNO_3$ electrolytes (53) but poorly in 1 M $LiPF_6$ propylene carbonate (54). Indeed, high CE_{avg-Li} values were observed for the former three (97.4, 97.9, and 98.1%, respectively; *SI Appendix*, Table S2) and a low CE_{avg} was found for the latter (84.7%; *SI Appendix*, Table S2). The CE_{avg-Li} in EL-0 to -4 was then measured. The $LiPF_6$ EC-DMC electrolyte (EL-0) showed a CE_{avg-Li} of 95.7% (Table 1). Replacing EC with a fluorinated EC such as FEC and DFEC significantly improved the CE_{avg-Li} to 98.3 and 97.8%, respectively. However, this beneficial effect was not observed for CF_3EC, which showed a very low CE_{avg-Li} of 54.2%. The EL-4 electrolyte with 3 wt% DTD additive showed the highest CE_{avg-Li} of 98.8%. The voltage curves of Li-Li asymmetric cell tests using EL-0 to -4 electrolytes can be seen in *SI Appendix*, Fig. S6.

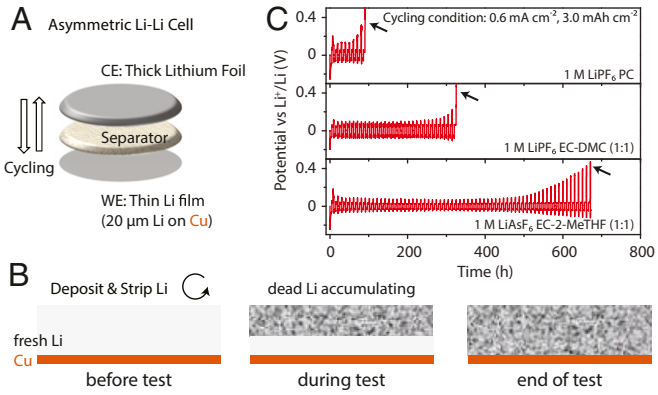

Fig. 4. Asymmetric Li-Li cell design and test. (*A*) Schematic illustration of an asymmetric Li-Li cell consisting of a thin Li-metal electrode (working electrode [WE]), a separator, and a thick Li-metal electrode (counter electrode [CE]). In the first half-cycle, a fixed amount of Li is electrochemically deposited onto the thin Li electrode, and then this amount is stripped and deposited repeatedly. (*B*) Evolution of the Li film on the thin Li electrode (WE) during the test. The Li originally coated on the Cu substrate was gradually consumed by the side reactions, and some of it becomes "dead Li" insulated by a thick SEI layer. (*C*) Voltage curves of three selected examples of the Li-Li asymmetric cell tests. The cycling current density was 0.6 mA cm^{-2}. The cycling areal capacity is 3.0 mAh cm^{-2}. Li was first deposited on the thin Li electrode and then stripped. The final voltage spikes denoted by the black arrows indicate the end of the tests when there is no Li available for stripping anymore and the absence of short-circuits during the tests. Longer cycle time before the voltage spikes indicate higher CE_{avg-Li}, based on Eq. **4**.

It is important to note that the above results were obtained in the absence of any significant applied pressure. Pressure applied to Li-metal cells may improve their cycling stability (55). Indeed, we found that when a 100-pounds per square inch (PSI) stack pressure is applied, the $CE_{avg\text{-}Li}$ further improved to 99.1%. The details of the measurement of $CE_{avg\text{-}Li}$ vs. stack pressure appear in *SI Appendix*, Fig. S7.

We now compare the present CE results to the highest reported values in literature. $CE_{avg\text{-}Li}$ >99.0% has been previously reported for 4 M lithium bis(fluorosulfonyl)imide (LiFSI) in DME (21), 1.2 M LiFSI DMC/bis(2,2,2-trifluoroethyl) ether (BTFE) (56), and 1.2 M triethyl phosphate (TEP)/BTFE electrolytes (49), measured using a 10-cycle average method in Li-Cu cells as described in detail in ref. 21. We prepared these electrolytes using battery-grade reagents and measured the 10-cycle $CE_{avg\text{-}Li}$ using the same procedure, along with our best-performing EL-4 electrolyte (all at 1 mA cm^{-2} current density). Four cells were tested in each case. The EL-4 electrolyte showed a 10-cycle $CE_{avg\text{-}Li}$ of 98.4 ± 0.2% (average CE ± SD; highest CE, 98.7%), slightly lower than 4 M LiFSI-DME (98.6 ± 0.5%; highest, 99.0%) and 1.2 M LiFSI DMC/BTFE (99.1 ± 0.05%; highest, 99.2%). The 1.2 M LiFSI TEP/BTFE electrolyte showed low $CE_{avg\text{-}Li}$ (87.7 ± 3.3%) in our 10-cycle tests for unknown reasons. However, despite the high $CE_{avg\text{-}Li}$ of 4 M LiFSI-DME and 1.2 M LiFSI DMC/BTFE, these two electrolytes are not compatible with high-voltage cathodes necessary to achieve high energy densities. When used in Li||$LiCoO_2$ cells charged to 4.5 V, rapid capacity decay occurred (*SI Appendix*, Fig. S8), likely due to electrolyte oxidation or aluminum/stainless steel corrosion by LiFSI, as previously mentioned by ref. 49. This leaves EL-4 as one of very few electrolytes that work well with both the Li-metal anode and a high-voltage cathode, as we later demonstrate for lithium nickel manganese aluminum oxide (NCA) and lithium-rich and manganese-rich-NMC (LMR-NMC) cathodes as well. A recently reported dual-salt LiDFOB/$LiBF_4$ electrolyte in FEC/diethyl carbonate (DEC) (1/2 vol/vol) could work at 4.5 V and enabled a cycle life of 90 cycles for anode-free batteries (57). We also measured the 10-cycle $CE_{avg\text{-}Li}$ of this electrolyte, which was 97.4 ± 1.4% (highest, 98.4%), slightly lower than that of the EL-4 (98.4 ± 0.2%; highest CE, 98.7%).

The asymmetric Li-Li cell test provides a useful platform to evaluate and compare the effectiveness of different electrolyte components (salts, solvents, and additives). It is able to quantify both the CE and areal-specific resistance (ASR) of the Li-metal electrodes, whereas the conventional symmetric Li-Li cell tests can only quantify ASR. Furthermore, "soft" short-circuits can be difficult to differentiate from a low ASR in symmetric Li-Li cells, whereas the asymmetric configuration yields unrealistically high CE (i.e., outliers) when short-circuits are present. The asymmetric Li-Li cell test is also more directly relevant to practical applications than the widely used asymmetric Li-Cu (or Ni, or stainless steel) cell test in which Li is deposited on bare-metal current collector, since the use of thin Li anodes in a full cell in most instances will provide a better compromise between energy density and cycle life than the so-called "anode-free" configuration, where deposition occurs on a metal current collector. One limitation of the asymmetric Li-Li cell test is that it cannot evaluate the CE at each cycle, which can be obtained from the Li-Cu cell test (*SI Appendix*, Fig. S9). We suggest that these tests may be used in a complementary way to evaluate the cycling of Li-metal anode.

Table 1. Average CE of Li anodes in different electrolytes

Lithium salt, 1 M	Solvents and additives	*N*, cycles	CE_{avg}, %
$LiPF_6$	EC-DMC (1:1 v), EL-0	32	95.7
$LiPF_6$	FEC-DMC (1:1 v), EL-1	80	98.3
$LiPF_6$	DFEC-DMC (1:1 v), EL-2	62	97.8
$LiPF_6$	CF_3EC-DMC (1:1 v), EL-3	3	54.2
$LiPF_6$	FEC-DMC (1:1 v) + DTD, EL-4	114	98.8
With 100-PSI stack pressure, 30-μm Li working electrode			
$LiPF_6$	FEC-DMC (1:1 v) + DTD, EL-4	225	99.1

Test conditions were as follows: 0.6 mA cm^{-2} current density and 3.0 mAh cm^{-2} cycling areal capacity.

Descriptors for Effective SEIs. The comparison between EC, FEC, DFEC, and CF_3EC provides insights into what makes FEC (and the SEIs formed in FEC-containing electrolytes) more favorable for stable Li-metal anode cycling. While a LiF-rich SEI is needed, there are likely other critical factors in determining the effectiveness of the SEI and stable cycling of Li-metal anode.

In order to formulate the structure–property relationship between the electrolyte components and their function in cycling, we propose two descriptors that are key for a high-performance, self-formed SEI. The two key factors are 1) the fraction of ionic compounds in the SEI, which is needed for ensuring low electronic conductivity (58), and 2) the compactness of the SEI, which will control the morphology and packing density of the inorganic and organic phases. Here, we propose using the number of electrons transferred from the Li surface to the electrolyte molecule, obtained from the DFT calculations, as a descriptor for the fraction of ionic compounds in the SEI. A higher number of electrons transferred from Li to the organic compound would lead to formation of more Li^+ and anions, i.e., formation of more ionic compounds, as shown in Table 2. On the other hand, describing the compactness and morphology of the SEI is a more challenging problem. We propose that the volume of the organic species left behind from the decomposition is a good descriptor, to a first approximation, to describe the ability to form a compact SEI. Volume of species determines the size of pores formed and also the number and size of the interfaces formed for Li^+ conduction. This volume can be approximately quantified by the Bader volume of the largest SEI species, typically the organometallic salt component, again obtained from the DFT calculations. More details on the rationale behind the two descriptors are discussed in *SI Appendix*. These two descriptors, used in conjunction, can rationalize the experimentally observed trends. Based on the descriptor for the fraction of ionic compounds in the SEI, among the present fluorinated solvents, the trend is CF_3EC << FEC < DFEC. Using just this descriptor, we would conclude that DFEC leads to a more ionic SEI. However, when comparing the descriptor for compactness of the SEI, the incomplete decomposition of DFEC leads to much larger moieties for DFEC than FEC. These two factors taken together indicate that FEC performs better overall due to a combination of an ionic and compact SEI. Note that the cosolvent DMC used in our experiments is less reactive than FEC, DFEC, and DTD. This means that these compounds would be preferentially decomposed on Li.

The case of DTD is special and suggests a different strategy to enrich the LiF content in the SEI. Unlike the other electrolyte molecules considered, DTD decomposes along with $LiPF_6$ to form LiF, PF_5, ethane-1,2-diolate (similar to one of the decomposition products of FEC), and SO_2^{2-} anion. The latter eventually leads to the formation of Li_2SO_3 and $ROSO_2Li$, as observed by XPS. For the two descriptors identified, DTD leads to the formation of a more ionic SEI, while maintaining high SEI compactness quite similar to FEC. We attribute the improved behavior seen in the FEC-DTD case to increased LiF, Li_2CO_3 and sulfite formation from the DTD addition, as confirmed by the XPS results. The interfaces between LiF, Li_2CO_3, and sulfite species may be more facile for Li^+ conduction. A compact and highly ionic SEI is favorable for uniform Li deposition that leads to dense Li film (Fig. 3). Without these properties, Li would be

Table 2. Theoretical descriptors for solvent decomposition on Li metal

Solvent	Electrons transferred	Bader volume of largest SEI species, Å^3
DMC	2.0	145
EC	2.5	132
FEC	3.3	89
DFEC	4.4	125
CF_3EC	0.5	169
DTD	4.1	97

preferentially deposited at locations that are more conductive to Li ions, and the resulting film is less dense. Thus, these two descriptors together can provide rational design principles for the selection of electrolyte compounds that result in high-performing SEI.

Full Cell Tests with Li-Metal and High-Voltage Cathodes. The cycling performance of the thin Li-metal anodes in different electrolytes was further evaluated in Li (50 μm; areal capacity, 10.3 mAh cm^{-2})|| $LiCoO_2$ (areal capacity, ~4.2 mAh cm^{-2}) full cells. Three formation cycles were performed at 0.1 C before the long-term cycling tests at 0.2 C charge/0.5 C discharge between 4.5 and 3.0 V. The Li||$LiCoO_2$ full cells using the EL-4 electrolyte retained more than 80% of the initial capacity for 350 cycles, significantly better than those using EL-0 and EL-1 electrolytes (Fig. 5 *A*–*D*). When a 20-μm-thick Li anode was used (less Li excess), the Li||$LiCoO_2$ cell could still retain 80% of the initial capacity for about 130 cycles (*SI Appendix*, Fig. S10). This shows that thickness of Li provides an effective way to strike an application dependent tradeoff between cycle life and specific energy. Comparing results from EL-1 (FEC-DMC) and EL-4 (FEC-DMC + DTD), it is clear that simply having a high concentration of FEC in the electrolyte is not sufficient to enable long cycle life for Li-metal anodes or Li-metal full cells. The EL-4 electrolyte also worked well in a Li (50 μm)||NCA full cells (*SI Appendix*, Fig. S11), which provided a cycle life of 252 cycles when cycled at an even larger areal capacity (4.7 mAh cm^{-2} initially; average cycling areal capacity, 4.4 mAh cm^{-2}). EL-4 could also work with LMR-NMC charged to 4.85 V. Initial testing of a Li (50 μm)||LMR-NMC full cell shows stability to at least 20 cycles (*SI Appendix*, Fig. S12).

A close inspection of the CE reveals that the Li||$LiCoO_2$ full cells using the EL-4 electrolyte can sustain a very high average CE of >99.9% during cycling, whereas the CE for the cells using EL-0 and EL-1 electrolytes quickly dropped below 99% (Fig. 5 *A*, *Middle*). We want to point out that this CE should not be mistaken as the CE_{avg} for the Li-metal anode because these cells contain an excess amount of Li and are cathode-limited initially. At the early stage of cycling, the measured CE (Fig. 5 *A*, *Middle*) determines the CE of the cathode material, i.e., $LiCoO_2$. After a certain number of cycles, the CE loss of the Li||$LiCoO_2$ cell reflects the capacity loss at the cathode, the Li-metal anode, and the side reactions, which occur at both. It is more accurate to use the following equation, which provides a lower bound for $CE_{avg\text{-}Li}$:

$$CE_{avg} = \frac{\sum Q_{discharge}}{\sum Q_{charge} + Q_{Li\ anode}}. \quad [5]$$

$Q_{Li\ anode}$ is the capacity of the 50-μm-thick Li anode. $\sum Q_{charge}$and $\sum Q_{discharge}$ are total capacity for Li deposition and stripping, respectively. The $CE_{avg\text{-}Li}$ was determined to be 99.0% after 350 cycles. Since $LiCoO_2$ will also lose capacity during cycling and the cells did not completely fail after 350 cycles, combining both effects, the $CE_{avg\text{-}Li}$ for EL-4 in the Li||$LiCoO_2$ cells would clearly be >99.0%.

We also observed a correlation between capacity decay and ASR increase (Fig. 5 *A*, *Top* and *Bottom*). The ASR was measured at the beginning of each discharge half-cycle, which equals the change in cell voltage (V) divided by the current density (mA cm^{-2}). The Li||$LiCoO_2$ cells using EL-4 (FEC-DMC + DTD) showed the slowest capacity decay and ASR increase. This result can be understood in terms of 1) FEC and DTD can both decompose to form an highly ionic yet compact SEI (Table 2) and 2) Li_2SO_3 and RSO_3Li were increasingly incorporated into the SEI as the cells were cycled, as shown by XPS (*SI Appendix*,

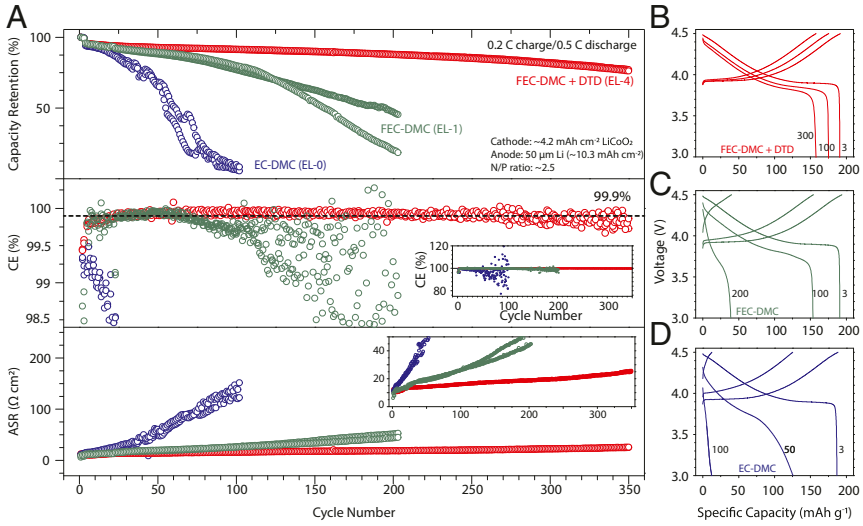

Fig. 5. Electrochemical tests of $LiCoO_2$-Li full cells. (*A*) Capacity retention (*Top*), CE (*Middle*), and ASR (*Bottom*) of the Li||$LiCoO_2$ full cells containing 1 M $LiPF_6$ EC-DMC (EL-0), 1 M $LiPF_6$ FEC-DMC (EL-1), and 1 M $LiPF_6$ FEC-DMC + DTD (EL-4) electrolytes, respectively. Results from two cells in each case are shown. ASR was measured at the beginning of each discharge half-cycle. The batteries were first cycled at 0.1 C for three cycles and then charged at 0.2 C and discharged at 0.5 C repeatedly between 4.5 and 3.0 V. The $LiCoO_2$ electrodes are ~23 mg cm^{-2} in mass loading and ~4.2 mAh cm^{-2} in areal capacity. The Li electrodes are 50 μm in thickness and 10.3 mAh cm^{-2} in areal capacity. EL-4 electrolyte enables the best capacity retention, highest average CE, and the lowest ASR during cycling. *Inset* in *A*, *Middle* (CE vs. cycle number) is the same plot with a larger *y*-axis scale. *Inset* in the *A*, *Bottom* (ASR vs. cycle number) is the same plot with a smaller *y*-axis scale. *B*–*D* are voltage profiles of the Li||$LiCoO_2$ full cells at different number of cycles using EL-4, EL-1, and EL-0 electrolytes.

ENGINEERING

Fig. S2). The interface between LiF and the sulfite species are facile for Li^+ conduction and thus limits the ASR growth.

The performance of the Li|$LiCoO_2$ (Fig. 5) and Li|NCA cells (*SI Appendix*, Fig. S11) with the EL-4 electrolyte is among the best to date for Li-metal rechargeable batteries. We compared our results with others using an updated version of the "ARPA-E plot" (ARPA-E: Advanced Research Projects Agency–Energy) previously shown in ref. 1 (Fig. 6). The data points in the plot were analyzed in terms of four parameters: cumulative capacity plated (Ah cm^{-2}), plated current density (mA cm^{-2}), per-cycle areal capacity (mAh cm^{-2}), and fraction of Li passed per cycle (F_p). To have a fair comparison, we chose to compare only results that met the following criteria: 1) from Li||intercalation-cathode full cells using liquid electrolytes; 2) Li SEIs self-formed from the decomposition of the electrolyte constituents; and 3) no other assisted approaches adopted, such as 3D current collector or Li-metal surface coating. Compared with previous literature, our work stands out for the highest cumulative capacity plated (up to 1.2 Ah cm^{-2} for point 25), high F_p ($F_p = 0.42$ for point 24; $F_p = 0.23$ for point 25; $F_p = 0.30$ for point 26), high per-cycle areal capacity (>3.4 mAh cm^{-2} for points 24 and 25 and 4.4 mAh cm^{-2} for point 26), which means higher energy density based on the analysis shown in Fig. 1. The data points in red in Fig. 1 (i.e., low F_p values) are from cells having relatively low overall energy density and far from meeting the US Department of Energy (DOE) goals (point 1 and 2, green color, $F_p \geq 0.8$). In this work, we have demonstrated cells using a 20-μm Li anode (negative-to-positive electrode capacity ratio [n/p], ~1) lasting 130 cycles and cells using a 50-μm Li anode (n/p, ~2.5) lasting 350 cycles at practical current densities, cathode loadings, and a relatively lean electrolyte condition (<9.4 μL mAh^{-1}). Further, the voltage profiles clearly rule out the possibility of a soft short. Finally, our cells using the EL-4 electrolyte exhibit linear capacity fade, distinct from the typically observed nonlinear drop in capacity after a few cycles (which usually indicates severe dead Li accumulation and/or electrolyte dry-out).

Conclusions

We have shown that structurally similar F-containing compounds (FEC, DFEC, and CF_3EC) can decompose differently and do not necessarily lead to formation of a LiF-rich SEI (FEC vs. DFEC and CF_3EC). Further, simply using a high concentration of FEC in the electrolyte to produce a LiF-rich SEI is not sufficient to enable long cycle life for Li-metal full cells using thin Li-metal anodes. It is discovered that the combination of FEC and DTD can enrich the SEI with ionic compounds such as LiF, Li_2CO_3, and Li_2SO_3 and maintain its high density, which promotes dense Li electrodeposition and high CE and slows down ASR growth during cycling. Li||$LiCoO_2$ full cells with small Li excess (n/p, ~2.5) demonstrated stable cycling performance over 350 cycles at practically relevant areal capacity, C-rates, and a relatively lean electrolyte condition. This work establishes design principles for well-functioning SEI to improve the performance of Li-metal rechargeable batteries.

Materials and Methods

Materials. The 20-μm-thick Li film coated on Cu foil was purchased from Honjo, Japan. The 50-μm-thick Li film coated on Cu foil was purchased from China Lithium Energy Co., Ltd. The electrolytes were prepared by (Shanghai Songjing New-Energy Technology) using battery-grade reagents, except EL-2 because DFEC was only available at 95% purity (from BOCSCI Inc.). Ionic conductivities of the prepared electrolytes are shown in *SI Appendix*, Table S3. The $LiCoO_2$ electrode sheets were prepared by coating the slurry of $LiCoO_2$ cathode powder (LC-95; Hunan Shanshan), carbon black, and polyvinylidene difluoride (weight ratio, 96:2:2) on aluminum foils. The electrodes were calendared to ~60 μm. The mass loading of $LiCoO_2$ was ~23 mg cm^{-2}.

Characterizations. XPS measurements were carried out using a Kratos X-ray photoelectron spectrometer. To avoid electrode contaminations caused by exposure to air, the Li electrodes were rinsed using fresh DMC, dried, sealed in a specialized holder inside the Ar-filled glovebox, and then transferred into the chamber of the XPS instrument. SEM characterizations were carried out using a Phenom-Pro scanning electron microscope installed inside an Ar-filled glovebox. The cross-section of the deposited Li films were prepared by slowly tearing the electrodes. Using a razor blade to cut the electrodes is not advised because it easily deforms the soft Li metal and appears to "smooth out" the deposited Li films.

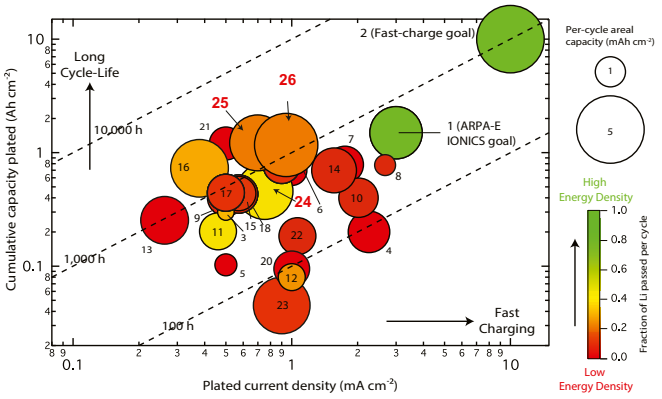

Fig. 6. Comparison of cycling performance of Li||intercalation-cathode full cells with self-formed SEI from liquid electrolytes. Data points 24, 25, and 26 in red are from current density. Points 1 and 2 are US DOE goals; 3 to 26 are results from Li||intercalation-cathode full cells with self-formed Li-SEI from liquid electrolytes but not assisted by any other Li-metal protection or modification approaches. See Dataset S1 for references and additional comments for each point. Data points 24 and 25 are from Li (20 μm)||$LiCoO_2$ (4.2 mAh cm^{-2}) and Li (50 μm)||$LiCoO_2$ (4.2 mAh cm^{-2}) full cells, respectively. Data point 26 is from a Li (50 μm)||$LiNi_{0.8}Co_{0.15}Al_{0.05}O_2$ (4.7 mAh cm^{-2}) full cell. EL-4 electrolyte (1 M $LiPF_6$ FEC-DMC + 3 wt% DTD) is used. Compared with previous work using liquid electrolytes, our work stands out for one of the highest cumulative capacity plated (~1.2 Ah cm^{-2}) (i.e., long cycle life, up to 350 cycles for 80% capacity retention for point 25) when the cell is cycling at a large per-cycle areal capacity (average, ~3.4 mAh cm^{-2}). The specific-energy density of the point 25 cell is >350 Wh kg^{-1} according to the analysis in Fig. 1.

Electrochemical Measurements. Electrochemical performances were measured using CR2025 coin-type cells. The Li-metal full cells were assembled using a $LiCoO_2$ cathode, a thin Li-metal anode (20 or 50 μm in thickness) and one piece of polyethylene separator, and 45 μL of electrolyte per cell. Some electrolyte overflowed from the coin cells when they were being sealed under pressure. Therefore, the actual amount of electrolyte inside the coin cell is less than 45 μL. The size of the cathode and the Li-metal anode are 12 and 14 mm in diameter, respectively. We did not apply external pressure to the coin cell. Electrochemical tests were performed using battery cyclers (10/1.0 mA version, 0.05% current/voltage resolution; BTS4000-5V; Shenzhen Neware). The coin cells were cycled inside temperature chambers set at 30 ± 0.5 °C. The Li-metal full cells were first cycled at 0.1 C between 4.5 to 3.0 V for three cycles and then charged at 0.2 C and discharged at 0.5 C, repeatedly; 1 C equals ~3.7 mA cm^{-2}.

DFT Simulations. Self-consistent DFT calculations were performed using the real-space projector-augmented wave method (59, 60) implemented in the GPAW code (DFT Python code based on the projector-augmented wave method and the atomic simulation environment) (61, 62) and employing the PBE (programming by example) exchange-correlation functional (63). We performed the DFT calculations on the Li (100), (110), and (111) surfaces (*SI Appendix*, Fig. S13). The results suggest that the surface-energy effects do not significantly affect the decomposition pathway for solvent decomposition on Li. The Li surfaces consisted of four layers with the bottom two layers constrained at the bulk lattice constants. Each layer consisted of a 3 × 3 Li unit cell. The solvent molecule along with Li^+ and PF_6^- ions were placed on top of the Li surface, and the structure was allowed to relax to determine the decomposition. Periodic boundary conditions were used for x and y directions, and a vacuum of 10 Å was used in the z direction perpendicular to the surface on both sides of the slab. A real-space grid spacing of 0.16 Å was used, and the Brillouin zone was sampled using the Monkhorst–Pack scheme (64) with a k-point grid of 6 × 6 × 1. All simulations were converged to a force <0.05 eV $Å^{-1}$. Lastly, Bader analysis (65) was used to determine the

amount of charge transferred from the Li to the solvent during the decomposition and also volumes of the various decomposed species.

Data Availability. All study data are included in the article and supporting information.

ACKNOWLEDGMENTS. This work was supported by the Assistant Secretary for Energy Efficiency and Renewable Energy, Office of Vehicle Technologies of the US DOE through Advanced Battery Materials Research Program Contract DE-EE0007810, and supported by the start-up fund of the Shanghai Jiao Tong University and the Natural Science Foundation of Shanghai, the Science and Technology Commission Shanghai Municipality (Grant 19ZR1475100; to L.S.L).

1. P. Albertus, S. Babinec, S. Litzelman, A. Newman, Status and challenges in enabling the lithium metal electrode for high-energy and low-cost rechargeable batteries. *Nat. Energy* **3**, 16–21 (2018).
2. J.-G. Zhang, W. Xu, W. A. Henderson, *Lithium Metal Anodes and Rechargeable Lithium Metal Batteries*, (Springer International Publishing, ed. 1, 2017).
3. D. Lin, Y. Liu, Y. Cui, Reviving the lithium metal anode for high-energy batteries. *Nat. Nanotechnol.* **12**, 194–206 (2017).
4. K. N. Wood, M. Noked, N. P. Dasgupta, Lithium metal anodes: Toward an improved understanding of coupled morphological, electrochemical, and mechanical behavior. *ACS Energy Lett.* **2**, 664–672 (2017).
5. D. Lin *et al.*, Layered reduced graphene oxide with nanoscale interlayer gaps as a stable host for lithium metal anodes. *Nat. Nanotechnol.* **11**, 626–632 (2016).
6. C.-P. Yang, Y.-X. Yin, S.-F. Zhang, N.-W. Li, Y.-G. Guo, Accommodating lithium into 3D current collectors with a submicron skeleton towards long-life lithium metal anodes. *Nat. Commun.* **6**, 8058 (2015).
7. P. Bai *et al.*, Interactions between lithium growths and nanoporous ceramic separators. *Joule* **2**, 2434–2449 (2018).
8. C.-Z. Zhao *et al.*, An ion redistributor for dendrite-free lithium metal anodes. *Sci. Adv.* **4**, eaat3446 (2018).
9. Y. Liu *et al.*, Making Li-metal electrodes rechargeable by controlling the dendrite growth direction. *Nat. Energy* **2**, 17083 (2017).
10. J. Zheng *et al.*, Electrolyte additive enabled fast charging and stable cycling lithium metal batteries. *Nat. Energy* **2**, 17012 (2017).
11. X. Ren *et al.*, Guided lithium metal deposition and improved lithium Coulombic efficiency through synergistic effects of $LiAsF_6$ and cyclic carbonate additives. *ACS Energy Lett.* **3**, 14–19 (2018).
12. X.-Q. Zhang, X.-B. Cheng, X. Chen, C. Yan, Q. Zhang, Fluoroethylene carbonate additives to render uniform Li deposits in lithium metal batteries. *Adv. Funct. Mater.* **27**, 1605989 (2017).
13. J. Qian *et al.*, Dendrite-free Li deposition using trace-amounts of water as an electrolyte additive. *Nano Energy* **15**, 135–144 (2015).
14. M. S. Kim *et al.*, Langmuir–Blodgett artificial solid-electrolyte interphases for practical lithium metal batteries. *Nat. Energy* **3**, 889–898 (2018).
15. N.-W. Li, Y.-X. Yin, C.-P. Yang, Y.-G. Guo, An artificial solid electrolyte interphase layer for stable lithium metal anodes. *Adv. Mater.* **28**, 1853–1858 (2016).
16. Z. Tu *et al.*, Fast ion transport at solid–solid interfaces in hybrid battery anodes. *Nat. Energy* **3**, 310–316 (2018).
17. X. Liang *et al.*, A facile surface chemistry route to a stabilized lithium metal anode. *Nat. Energy* **2**, 17119 (2017).
18. L. Suo *et al.*, Fluorine-donating electrolytes enable highly reversible 5-V-class Li metal batteries. *Proc. Natl. Acad. Sci. U.S.A.* **115**, 1156–1161 (2018).
19. X. Fan *et al.*, Highly fluorinated interphases enable high-voltage Li-metal batteries. *Chem* **4**, 174–185 (2018).
20. J. Qian *et al.*, High rate and stable cycling of lithium metal anode. *Nat. Commun.* **6**, 6362 (2015).
21. B. D. Adams, J. Zheng, X. Ren, W. Xu, J.-G. Zhang, Accurate determination of Coulombic efficiency for lithium metal anodes and lithium metal batteries. *Adv. Energy Mater.* **8**, 1702097 (2018).
22. X. Han *et al.*, Negating interfacial impedance in garnet-based solid-state Li metal batteries. *Nat. Mater.* **16**, 572–579 (2017).
23. H. Duan *et al.*, Dendrite-free Li-metal battery enabled by a thin asymmetric solid electrolyte with engineered layers. *J. Am. Chem. Soc.* **140**, 82–85 (2018).
24. J. Li, C. Ma, M. Chi, C. Liang, N. J. Dudney, Solid electrolyte: The key for high-voltage lithium batteries. *Adv. Energy Mater.* **5**, 1401408 (2015).
25. P. Bai, J. Li, F. R. Brushett, M. Z. Bazant, Transition of lithium growth mechanisms in liquid electrolytes. *Energy Environ. Sci.* **9**, 3221–3229 (2016).
26. A. Kushima *et al.*, Liquid cell transmission electron microscopy observation of lithium metal growth and dissolution: Root growth, dead lithium and lithium flotsams. *Nano Energy* **32**, 271–279 (2017).
27. Y. Li *et al.*, Atomic structure of sensitive battery materials and interfaces revealed by cryo-electron microscopy. *Science* **358**, 506–510 (2017).
28. Y. Li *et al.*, Correlating structure and function of battery interphases at atomic resolution using cryoelectron microscopy. *Joule* **2**, 2167–2177 (2018).
29. Y. Lu, Z. Tu, L. A. Archer, Stable lithium electrodeposition in liquid and nanoporous solid electrolytes. *Nat. Mater.* **13**, 961–969 (2014).
30. E. Markevich, G. Salitra, F. Chesneau, M. Schmidt, D. Aurbach, Very stable lithium metal stripping–plating at a high rate and high areal capacity in fluoroethylene carbonate-based organic electrolyte solution. *ACS Energy Lett.* **2**, 1321–1326 (2017).
31. Y. Lu, Z. Tu, J. Shu, L. A. Archer, Stable lithium electrodeposition in salt-reinforced electrolytes. *J. Power Sources* **279**, 413–418 (2015).
32. F. Wu *et al.*, Lithium iodide as a promising electrolyte additive for lithium-sulfur batteries: Mechanisms of performance enhancement. *Adv. Mater.* **27**, 101–108 (2015).
33. C. Yan *et al.*, Lithium nitrate solvation chemistry in carbonate electrolyte sustains high-voltage lithium metal batteries. *Angew. Chem. Int. Ed. Engl.* **57**, 14055–14059 (2018).
34. W. Li *et al.*, The synergetic effect of lithium polysulfide and lithium nitrate to prevent lithium dendrite growth. *Nat. Commun.* **6**, 7436 (2015).
35. L. Ma, M. S. Kim, L. A. Archer, Stable artificial solid electrolyte interphases for lithium batteries. *Chem. Mater.* **29**, 4181–4189 (2017).
36. M. Ishikawa, M. Morita, Y. Matsuda, In situ scanning vibrating electrode technique for lithium metal anodes. *J. Power Sources* **68**, 501–505 (1997).
37. E. Kazyak, K. N. Wood, N. P. Dasgupta, Improved cycle life and stability of lithium metal anodes through ultrathin atomic layer deposition surface treatments. *Chem. Mater.* **27**, 6457–6462 (2015).
38. Y. Liu *et al.*, An artificial solid electrolyte interphase with high Li-Ion conductivity, mechanical strength, and flexibility for stable lithium metal anodes. *Adv. Mater.* **29**, 1605531 (2017).
39. L. Weinstein, W. Yourey, J. Gural, G. G. Amatucci, Electrochemical impedance spectroscopy of electrochemically self-assembled lithium–iodine batteries. *J. Electrochem. Soc.* **155**, A590–A598 (2008).
40. W. K. Behl, D. T. Chin, Electrochemical overcharge protection of rechargeable lithium batteries: I. Kinetics of iodide/tri-iodide/iodine redox reactions on platinum in solutions. *J. Electrochem. Soc.* **135**, 16–21 (1988).
41. W. K. Behl, D. T. Chin, Electrochemical overcharge protection of rechargeable lithium batteries: II. Effect of lithium iodide-iodine additives on the behavior of lithium electrode in solutions. *J. Electrochem. Soc.* **135**, 21–25 (1988).
42. W. K. Behl, Anodic oxidation of lithium bromide in tetrahydrofuran solutions. *J. Electrochem. Soc.* **136**, 2305–2310 (1989).
43. X. Fan *et al.*, Non-flammable electrolyte enables Li-metal batteries with aggressive cathode chemistries. *Nat. Nanotechnol.* **13**, 715–722 (2018).
44. J.-Y. Hwang, S.-J. Park, C. S. Yoon, Y.-K. Sun, Customizing a Li–metal battery that survives practical operating conditions for electric vehicle applications. *Energy Environ. Sci.* **12**, 2174–2184 (2019).
45. G. Salitra *et al.*, High-performance cells containing lithium metal anodes, $LiNi_{0.6}Co_{0.2}Mn_{0.2}O_2$ (NCM 622) cathodes, and fluoroethylene carbonate-based electrolyte solution with practical loading. *ACS Appl. Mater. Interfaces* **10**, 19773–19782 (2018).
46. J. Xia, R. Petibon, A. Xiao, W. M. Lamanna, J. R. Dahn, Some fluorinated carbonates as electrolyte additives for Li(Ni0.4Mn0.4Co0.2)O2/graphite pouch cells. *J. Electrochem. Soc.* **163**, A1637–A1645 (2016).
47. J. Shen, H. Chen, L. Yu, D. Huang, Z. Luo, 4, 5-difluoro-1, 3-dioxolan-2-one as an film forming additive on $LiNi_{0.8}Co_{0.15}Al_{0.05}O_2$/SiO@C full cells. *J. Electroanal. Chem. (Lausanne)* **834**, 1–7 (2019).
48. J. Xia, N. N. Sinha, L. P. Chen, J. R. Dahn, A comparative study of a family of sulfate electrolyte additives. *J. Electrochem. Soc.* **161**, A264–A274 (2014).
49. S. Chen *et al.*, High-efficiency lithium metal batteries with fire-retardant electrolytes. *Joule* **2**, 1548–1558 (2018).
50. C. Fang *et al.*, Quantifying inactive lithium in lithium metal batteries. *Nature* **572**, 511–515 (2019).
51. W. Xianming, E. Yasukawa, S. Kasuya, Electrochemical properties of tetrahydropyran-based ternary electrolytes for 4 V lithium metal rechargeable batteries. *Electrochim. Acta* **46**, 813–819 (2001).
52. J.-I. Yamaki, The development of lithium rechargeable batteries. *J. Power Sources* **20**, 3–7 (1987).
53. S. S. Zhang, Role of $LiNO_3$ in rechargeable lithium/sulfur battery. *Electrochim. Acta* **70**, 344–348 (2012).
54. F. Ding *et al.*, Effects of carbonate solvents and lithium salts on morphology and coulombic efficiency of lithium electrode. *J. Electrochem. Soc.* **160**, A1894–A1901 (2013).
55. C. Niu *et al.*, High-energy lithium metal pouch cells with limited anode swelling and long stable cycles. *Nat. Energy* **4**, 551–559 (2019).
56. S. Chen *et al.*, High-voltage lithium-metal batteries enabled by localized high-concentration electrolytes. *Adv. Mater.* **30**, e1706102 (2018).
57. R. Weber *et al.*, Long cycle life and dendrite-free lithium morphology in anode-free lithium pouch cells enabled by a dual-salt liquid electrolyte. *Nat. Energy* **4**, 683–689 (2019).
58. F. Han *et al.*, High electronic conductivity as the origin of lithium dendrite formation within solid electrolytes. *Nat. Energy* **4**, 187–196 (2019).
59. P. E. Blöchl, Projector augmented-wave method. *Phys. Rev. B Condens. Matter* **50**, 17953–17979 (1994).
60. G. Kresse, D. Joubert, From ultrasoft pseudopotentials to the projector augmented-wave method. *Phys. Rev. B Condens. Matter Mater. Phys.* **59**, 1758–1775 (1999).
61. J. J. Mortensen, L. B. Hansen, K. W. Jacobsen, Real-space grid implementation of the projector augmented wave method. *Phys. Rev. B Condens. Matter Mater. Phys.* **71**, 035109 (2005).
62. J. Enkovaara *et al.*, Electronic structure calculations with GPAW: A real-space implementation of the projector augmented-wave method. *J. Phys. Condens. Matter* **22**, 253202 (2010).
63. J. P. Perdew, K. Burke, M. Ernzerhof, Generalized gradient approximation made simple. *Phys. Rev. Lett.* **77**, 3865–3868 (1996).
64. H. J. Monkhorst, J. D. Pack, Special points for Brillouin-zone integrations. *Phys. Rev. B* **13**, 5188–5192 (1976).
65. W. Tang, E. Sanville, G. Henkelman, A grid-based Bader analysis algorithm without lattice bias. *J. Phys. Condens. Matter* **21**, 084204 (2009).